

Dispersive modeling of breaking waves on a slope

Jihwan Kim^a, Geir K. Pedersen^a, Finn Løvholt^{a,b}, Randall J. LeVeque^c

^a*University of Oslo, Department of Mathematics, Oslo, Norway*

^b*Norwegian Geotechnical Institute, Oslo, Norway*

^c*University of Washington, Department of Applied Mathematics, Seattle, USA*

Abstract

Keywords:

1. Introduction

Depth-averaged models are widely used in the study of the tsunamis, and the *nonlinear shallow water equations* are a robust model. The shallow water equations are a system of hyperbolic partial differential equations which can be
5 derived from the Navier-Stokes' equations assuming that the vertical velocity is negligible. This leads to a hydrostatic pressure and a uniform horizontal speed horizontal throughout the depth. If waves have long wavelength with respect to the depth of water, the shallow water equations is a robust and efficient physical model. The shallow water equations have been used and validated in
10 the study of tsunami events such as the 2004 Indian Ocena tsunami and the 2011 Tohoku tsunami. However, some details of the waves have not been accurately captured, and one of the reasons is that the dispersion of waves is not included in the shallow water equations.

The dispersion becomes important in several cases. When surface waves
15 travel a long distance with respect to the wavelength, for example, the dispersion of waves develops. As another case, the waves generated by the submarine landslides have relatively short wavelength compared to the waves generated by the earthquakes, and the dispersion should be considered for accuracy.

The *Boussinesq-type equations* are a class of depth-averaged models which
20 can handle short waves better than the shallow water equations. With additional

dispersion terms, the Boussinesq-type equations can address the dispersive motion of wave revolution. One of the limitations of the Boussinesq-type equations arises when a wave breaks near the shoreline. Without appropriate modifications, the numerical results show that the wave height continues to increase and
25 may result in numerical instabilities. For this reason, several thresholds have been suggested to determine the wave break. As the wave break is detected, the governing equations are switched to the shallow water equations.

2. Model Description

If waves are shorter, alternative wave models may be preferred which can
30 handle dispersive waves. The Boussinesq-type equations is a class of the depth-averaged model that can treat shorter waves more accurately than the shallow water equations. The Boussinesq-type wave models have been derived by retaining $\mathcal{O}(\epsilon)$ and $\mathcal{O}(\mu)$ terms, where ϵ and μ denote the ratio of wave amplitude to depth and the ratio of depth to wavelength respectively. Various models
35 have been suggested. The papers of Peregrine (1967) [1], Madsen and Sørensen (1992) [2], Nwogu (1993) [3], Lynett et al. (2002) [4], and Wei and Kirby (1995) [5] are representative examples.

In this work, a new numerical tool, called *WaveClaw*, is introduced. It is an extension of GEOCLAW [6]. That solves the Boussinesq-type equations
40 derived by Schäffer et al. (1993) [7]. The WAVECLAW is a hybrid of the finite volume and finite difference solvers with the operation splitting technique. The GEOCLAW software is a part of CLAWPACK [6] by LeVeque (1997) [8], George (2008) [9] and Berger et al. (2011) [10] which solves the nonlinear shallow water equations.

2.1.1. Boussinesq-type equations

Schäffer et al. (1993) [7] derived Boussinesq-type equations with an addition of a Padé approximation of the linear dispersion relation. The equations read

$$H_t + (Hu)_x = 0, \quad (1)$$

$$(1 - D)[(Hu)_t] + \left(Hu^2 + \frac{g}{2}H^2\right)_x - gHh_x - Bgh^2(h\eta_x)_{xx} = 0, \quad (2)$$

where the operator, D , is defined as

$$D(w) = \left(B + \frac{1}{2}\right)h^2w_{xx} - \frac{1}{6}h^3\left(\frac{w}{h}\right)_{xx}, \quad (3)$$

for any $w(x, t)$. In the above equations $H(x, t)$ and $u(x, t)$ are the total flow depth and velocity of the water, respectively, $h(x)$ is the still water depth, $\eta(x, t)$ is the surface elevation, and thus $H(x, t) = h(x) + \eta(x, t)$. Moreover, g is the
50 acceleration of gravity, and B is a dispersion parameter. Madsen and Sørensen (1992) [2] has chosen the parameter $B = 1/15$ from a Padé expansion of the linear dispersion analysis.

When $B = 0$, this set of the Boussinesq-type equations approximately reduces to that of Peregrine (1967) [1] as the linear dispersion relations are identical. However, unlike Peregrine's momentum equation the hydrostatic parts of
55 (2) are written in a conservative form. This difference will be observed in the numerical procedure and is further elaborated in Appendix A.

The WAVECLAW software solves the Boussinesq-type equations (1) and (2) numerically with a hybrid of the finite volume and finite difference methods.
60 There have been several studies on this type of hybrid schemes. For example, see Tisser et al. (2011) [11], Shi et al. (2012) [12] and Dutykh et al. (2013) [13].

To facilitate a fractional step method, as outlined below, we move the hydrostatic terms of (2) inside the $(1 - D)$ operator, while balancing with extra terms in the Ψ , to obtain

$$(1 - D)[(Hu)_t] + \left(Hu^2 + \frac{g}{2}H^2\right)_x - gHh_x = -\Psi(x, t), \quad (4)$$

where

$$\begin{aligned} \Psi(x, t) = & \left(B + \frac{1}{2} \right) h^2 \left((Hu^2)_x + gH\eta_x \right)_{xx} \\ & - \frac{1}{6} h^3 \left(\frac{(Hu^2)_x + gH\eta_x}{h} \right)_{xx} - Bgh^2 (h\eta_x)_{xx}. \end{aligned} \quad (5)$$

2.1.2. Numerical scheme

The equations (1) and (4) are written in a form that is conserves momentum to leading order in μ , but with the Ψ term as a pseudo source. Such equations may be solved by a *fractional step method* as described in LeVeque (2002) [14], for instance. First, it is observed that (4) may be formally rewritten as

$$(Hu)_t = - \left\{ \left(Hu^2 + \frac{g}{2} H^2 \right)_x - gHh_x \right\} - (1 - D)^{-1} \Psi(x, t), \quad (6)$$

At the first stage of the hybrid scheme, we integrate Hu over a time step taking into account all hydrostatic terms on the right hand side, namely those within the braces and dropping the source terms involving Ψ . When this is combined with the continuity equation (1) this simply corresponds to advancing NLSW equations one time step forward. To this end we employ from GEOCLAW. In the second stage, we retain the new H value, but integrate Hu (essentially being the momentum density) further from the first stage by solving

$$(1 - D) [(Hu)_t] = -\Psi. \quad (7)$$

Since the differential operator D contains spatial derivatives, a systems of difference equations must then be solved.

65 The spatial and time discretization should be carefully chosen for the stability of the second stage. In our numerical scheme, the second order centered scheme is used for the spatial discretization, and a four stage Runge-Kutta method is used for the time integration. The von Neumann stability analysis of this numerical scheme is outlined in Appendix B.

Suppose the spatial domain is divided into n grid cells with the spatial grid size Δx . Arrays of nodal values for flow depth and Hu , respectively, are defined

add a description of the NLSW procedure

as

$$\mathbf{H} = (H_1, H_2, \dots, H_n)^T,$$

$$\mathbf{M} = (H_1 u_1, H_2 u_2, \dots, H_n u_n)^T.$$

With time increment Δt the fourth order Runge-Kutta scheme can be written as follows,

$$\mathbf{M}^1 = \mathbf{M}, \quad \mathbf{M}^2 = \mathbf{M} + \frac{\Delta t}{2} \mathbf{S}^1, \quad \mathbf{M}^3 = \mathbf{M} + \frac{\Delta t}{2} \mathbf{S}^2, \quad \mathbf{M}^4 = \mathbf{M} + \Delta t \mathbf{S}^3,$$

where \mathbf{M}^k are intermediate value arrays and \mathbf{S}^k are correspondingly arrays for the time derivatives of Hu , obtained by solving

$$(I - \bar{D})\mathbf{S}^k = -\bar{\Psi}(\mathbf{H}, \mathbf{M}^k), \quad \text{for } k = 1, \dots, 4. \quad (8)$$

Here $\bar{\Psi}$ and \bar{D} represent centered spatial discretizations for the term Ψ and the operator D , respectively. These are given explicitly below. Finally the value of \mathbf{M} at the new time level is obtained by

$$\mathbf{M}^+ = \mathbf{M} + \frac{\Delta t}{6} [\mathbf{S}^1 + 2\mathbf{S}^2 + 2\mathbf{S}^3 + \mathbf{S}^4].$$

In (8), \bar{D} is a tri-diagonal $n \times n$ matrix with elements

$$\bar{D}_{i,i-1} = \frac{1}{\Delta x^2} \left[\left(B + \frac{1}{2} \right) h_i^2 - \frac{1}{6} \frac{h_i^3}{h_{i-1}} \right],$$

$$\bar{D}_{i,i} = \frac{1}{\Delta x^2} \left(-2B - \frac{2}{3} \right) h_i^2,$$

$$\bar{D}_{i,i+1} = \frac{1}{\Delta x^2} \left[\left(B + \frac{1}{2} \right) h_i^2 - \frac{1}{6} \frac{h_i^3}{h_{i+1}} \right].$$

How are values for H obtained in the steps; linear interpolation ?

Correspondingly, the i -th element of $\Psi(\bar{\mathbf{H}}, \mathbf{q})$ is

$$\begin{aligned}\bar{\Psi}_i = & \left(B + \frac{1}{2} \right) \frac{h_i^2}{2\Delta x^3} \left[\left(\frac{M_{i+2}^2}{H_{i+2}} - 2\frac{M_{i+1}^2}{H_{i+1}} + 2\frac{M_{i-1}^2}{H_{i-1}} - \frac{M_{i-2}^2}{H_{i-2}} \right) \right. \\ & \left. + g(H_{i+1}(\eta_{i+2} - \eta_i) - 2H_i(\eta_{i+1} - \eta_{i-1}) + H_{i-1}(\eta_i - \eta_{i-2})) \right] \\ & - \frac{1}{6} \frac{h_i^3}{2\Delta x^3} \left[\frac{M_{i+2}^2/H_{i+2} - M_i^2/H_i}{H_{i+1}} - 2\frac{M_{i+1}^2/H_{i+1} - M_{i-1}^2/H_{i-1}}{h_i} \right. \\ & \left. + \frac{M_i^2/H_i - M_{i-2}^2/H_{i-2}}{H_{i-1}} \right. \\ & \left. + g \left(\frac{H_{i+1}(\eta_{i+2} - \eta_i)}{H_{i+1}} - 2\frac{H_i(\eta_{i+1} - \eta_{i-1})}{h_i} + \frac{H_{i-1}(\eta_i - \eta_{i-2})}{H_{i-1}} \right) \right] \\ & - \frac{Bgh_i^2}{2\Delta x^3} (H_{i+1}(\eta_{i+2} - \eta_i) - 2H_i(\eta_{i+1} - \eta_{i-1}) + H_{i-1}(\eta_i - \eta_{i-2})),\end{aligned}$$

70 for $i = 1, 2, \dots, n$.

2.2. Models for comparison

The performance of the Boussinesq model presented here is assessed by comparison with numerical results from a full potential flow model which is described in Løvholt et al. (2013) [15] and references therein. The model is based on a
75 boundary integral technique and is run with fully nonlinear solitary wave solutions as initial conditions. During shoaling and breaking this model can describe the evolution of a plunger, but breaks down when the plunger reaches the free surface. Hence, the potential flow results are used to determine the point of breaking due to shoaling and to evaluate the evolution of amplitude and wave
80 shape of the current model until this point. For short we refer to the full potential model as the BIM (Boundary Integral Method) model.

Comparison with a pre-existing, fully nonlinear Boussinesq model is facilitated by the application of a Lagrangian model, described in Løvholt et al. (2013) [15]. Apart from the use of Lagrangian coordinates the equations employed in this model are similar to (1) and (2). They differ only concerning
85 the nonlinearities in the dispersion terms and that the dispersion optimization terms are added in a fully nonlinear fashion. Presently, the Lagrangian model

has no established bore capturing facility and is hence valid only to the point of breaking. Results from this model will be referred to as 'Serre', even though
 90 the dispersion enhancement is invoked.

Results for the Peregrine type Boussinesq equations are obtained by the GloBouss model. This is a dispersive tsunami propagation model which is based on Peregrine type equations and discretization on a staggered grid. Further details are found in Løvholt and Pedersen (2008) [16].

95 For comparison also the version of the FUNWAVE model is used ref

Finn, you need to fill in an accurate description of FUNWAVE

3. Wave Steepening and Breaking

Synolakis (1987) [17] performed a series of laboratory experiments for the run-up of solitary waves on uniform slopes.

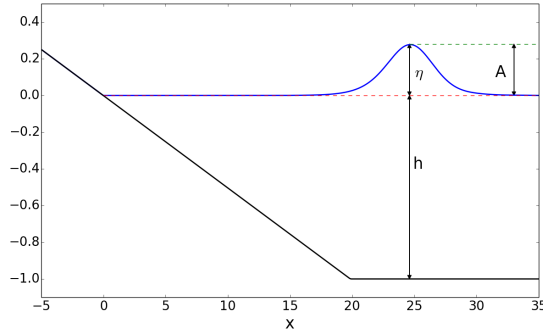


Figure 1: Set-up of a numerical test for Synolakis' experiments.

100 In this work, the main interests lie with the breaking wave cases, and one of the cases in Synolakis (1987) experiments is a solitary wave of $A/h = 0.28$ approaching a slope of 1 : 19.85. In Figure 1, the initial set-up for a test is shown.

In Figure 2, the laboratory measurements are shown with the computational
 105 results from the BIM model for a breaking wave case of Synolakis with $A/h = 0.28$ and 1 : 19.85 slope at $t^* = 15$. The non-dimensional time $t^* = t\sqrt{h/g}$ is

used in accordance with the laboratory experiments. The results are in good agreement.

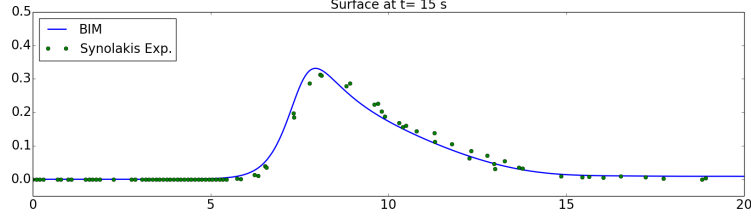


Figure 2: Comparison of the laboratory experiments and BIM at $t=15$ with $A/h = 0.28$ on a slope of 1 : 19.85.

Figure 3 shows the numerical results from BIM at $t = 17, 18$ and 18.6 . In
110 the BIM results a vertical front is observed at $x = 4.02$ m and $t = 18.6$ with the
maximum wave amplitude $A = 0.414$ m, and this shows similar results with the
analysis of Titov and Synolakis (1995) [18]. The ratio of amplitude to depth,
 A/h , is about 2.01 at the break point. The potential flow model cannot be run
much beyond the breaking points (until attachment of the plunger only) and
115 gives no information on the following bore propagation. In Figure 4, compu-
tations of the NLSW equations (present model without the second fractional
step) display a premature bore formation which checks the amplification during
the subsequent shoaling. As a consequence the amplitude in the NLSW simula-
tion is markedly smaller than that of the potential flow model when the latter
120 indicates breaking.

What is the result
of Titov and Syn-
olakis?

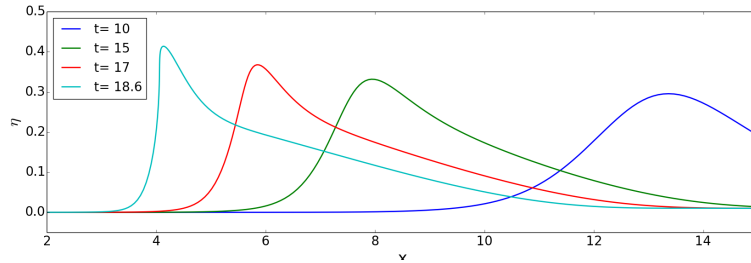


Figure 3: Computational results from BIM of a wave with $A/h = 0.28$ on a slope of 1 : 19.85. A vertical front is observed at $t = 18.6$.

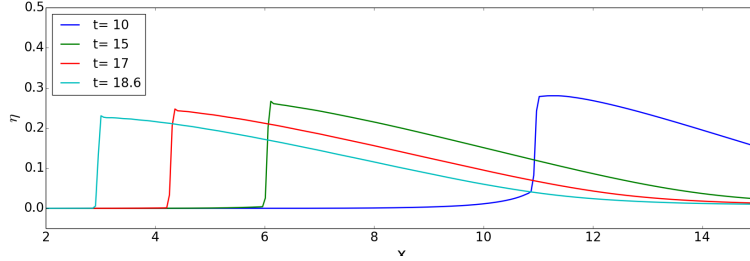


Figure 4: Computational results from SWE at $t = 10, 15, 17$ and 18.6 .

In their original formulation, the Boussinesq-type equations do not take into account the post-breaking motion. In order to combine breaking with the Boussinesq-type equations several strategies have been suggested. For example, Peregrine (1967) [1] used $A/h = 0.6$ as the break threshold, and also pointed out that this value reaches around 2 in some cases of laboratory experiments. Shi et. al (2012) [12] used $A/h = 0.8$ as the threshold for FUNWAVE based on the Froude analysis by Tonelli and Petti (2009) [19]. Schäffer et al. (1993) [7] introduced the concept of the *surface roller*. Lynett (2006) [20] investigated η_t/c , η_x , $u_{sxx}H^2/c$, and u_s/c , where $c = \sqrt{gH}$ and u_s = free surface speed, and then identified that the critical front slope (η_x) is the least sensitive breaking threshold. Tissier et al. (2012) [21] suggested a breaking decision model based on the surface roller, the maximal front angle and the Froude number. Løvholt et al. (2013) performed comprehensive numerical tests with different operational wave models, and studied the capability and limitation of the depth-integrated models. Matsuyama et al. (2007) [22] performed experiments of the wave propagation on various slope angles. They studied the wave breaking criteria and suggested

$$\frac{u_s}{c} = \frac{\eta}{H} - \frac{h}{3H} \left(H \frac{\partial^2 \eta}{\partial x^2} - 2 \left(\frac{\partial \eta}{\partial x} \right)^2 \right),$$

as a wave breaking criterion.

Although several criteria for the wave break have been suggested, it needs further studies to determine which criteria are more accurate. It should be noted that the criteria are sensitive, and the same value may not be applied

125 to other wave models in different wave experiments. At the same time, the computational efficiency and implementation should be considered in the wave break models.

4. Numerical Tests

4.1. Solitary wave propagation

In order to validate the numerical approach a solitary wave propagation is tested on a constant water depth. For the initial conditions, the analytic solitary wave solution of the Serre's equations is used since analytic solutions are unknown for the set (1) and (2). Solitary wave solutions to the Serre's equations are given as

$$\begin{aligned}\eta(x, t) &= A \operatorname{sech}^2(\kappa(x - ct)), \\ u(x, t) &= c \frac{\eta(x, t)}{h},\end{aligned}\tag{9}$$

where

$$\kappa = \frac{\sqrt{3h}}{2A\sqrt{A+h}}, \quad \text{and} \quad c = \sqrt{g(A+h)}.\tag{10}$$

130 In this expression, A and h are constants which represent the wave amplitude and the undisturbed water depth respectively, and this solution is only valid for a constant water depth.

In Figure 5, snapshots from the WAVECLAW's simulation is shown at $t = 0, 4, 8$ and 12 s with $\Delta x = 0.1$. For the initial conditions, the solution 9 is used
135 with $A = 0.2$, $h = 1$ and $g = 9.81$. The computational results are in a good agreement with the analytic solutions concerning height, shape and propagation speed. The amplitudes decreases very gently as the wave propagates. The discrepancy may be partially due to the numerical errors and partly to the fact that the analytic solution for Serre's equations satisfies the present Boussinesq-type equations only approximately.
140

In Figure 6a, the relative error of the maximum amplitude at $t = 12$,

$$E_\infty = \frac{|A_{comp} - A_{sol}|}{A_{sol}},$$

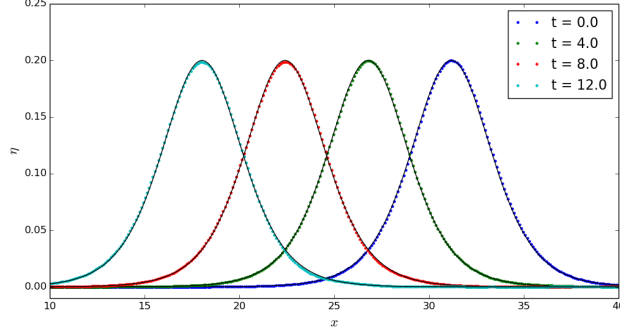


Figure 5: Snapshot of the analytic and computed solitary wave at $t = 0, 4, 8$ and 12 with $A/h = 0.2$. The wave propagates from right to left, and the analytic solutions are black solid lines.

is shown for Δx . The relative error for $A/h = 0.05$ is smaller than $A/h = 0.2$ because it is assumed that A/h is small in the derivation of the Boussinesq equations.

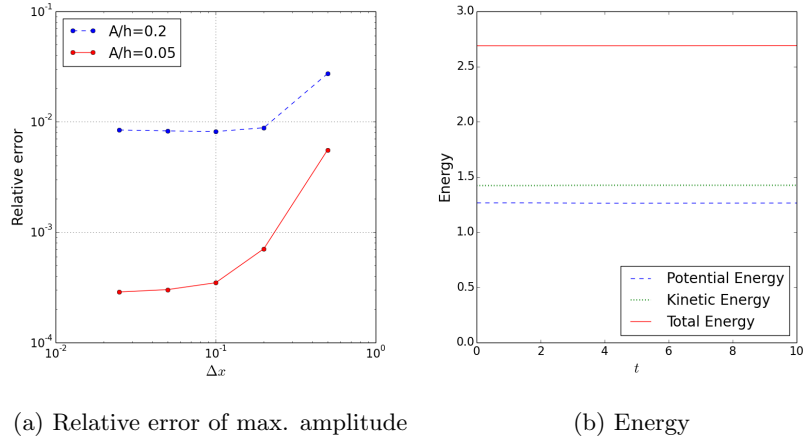


Figure 6: Relative error and energy of a soliton on a constant depth.

The wave energies for the NLSW and the Boussinesq equations are E_0 and

$E_0 + E_1$, respectively, where

$$E_0 = \frac{1}{2} (g\eta^2 + H\bar{u}^2), \quad (11)$$

$$E_1 = \frac{1}{6} H^3 \bar{u}_x^2 + \frac{1}{2} H^2 h_x \bar{u} \bar{u}_x + \frac{1}{2} H h_x^2 \bar{u}^2. \quad (12)$$

Details are given in Madsen et al. (1997) [23] and Appendix C, for example.

145 In Figure 6b, the energy of the solitary wave is shown with $A/h = 0.2$, and both the potential and kinetic energy remain constant, showing that the numerical procedure has negligible dissipation for smooth wave shapes.

4.2. Waves on a composite slope

A physical model was constructed at the Coastal Hydraulic Laboratory of the U.S. Army Corps of Engineers in order to address beach erosion and severe
150 flooding problems. The description of the benchmark problem can be found at CHL webpage [24]. The model beach consists of three piecewise linear slopes of 1:53, 1:150, and 1:13 with a vertical wall at the shoreline as shown in Figure 7. In the laboratory, the wavemaker was located at 23.23 m. The gauge data from
155 three cases are provided where the ratio A/h is equal to 0.038, 0.259 and 0.681 with $h = 21.8$ cm.

The second case with $A/h = 0.259$ have been compared with the numerical tests which were solved on a 400 point grid with no friction. To specify the incoming wave from the left boundary, the data at Gauge 4 were used for the
160 wave height, and the corresponding velocity (9) was applied.

In Figure 8, water surface elevations at the gauge 5, 7 and 8 are shown for $A/h = 0.269$ case. For the incoming waves, the agreement between the laboratory measurements and numerical simulations is good. For the reflecting waves, some differences are observed, Because the depth-averaged model is not
165 capable of describing the full interaction between the wave and the wall at the right boundary.

Friction forces are not applied in the numerical simulation which may become important at the shallow region. Although a difference in the wave speed is observed, the general wave pattern is well captured.

Geir: A very shallow region may yield important frictional effects? But, surely, the wave should break in the shallowest region?

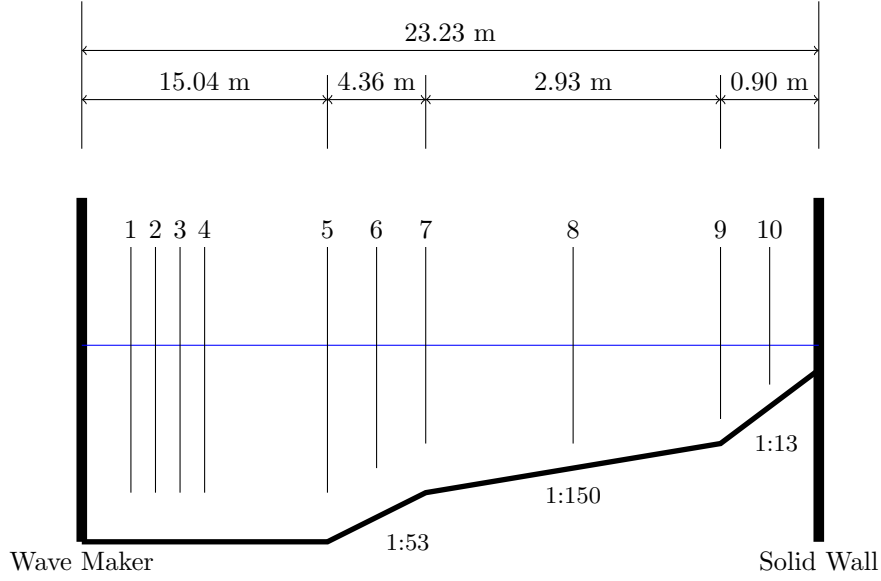


Figure 7: A sketch of the water tank

5. Breaking waves on a slope

The set-up of the wave tank follows the laboratory experiments by Synolakis (1987) [17]. The wave tank is assumed to have one horizontal direction, and the bathymetry is composed of a horizontal bottom and a uniform slope as shown in Figure 1. A solitary wave of $A/h = 0.28$ is generated at the right side and propagates to the shore on the left side.

In the measurement of Synolakis (1987), $t = 0$ was set when the distance from the wave crest to the toe of the slope is equal to L , where L is given as

$$L = \sqrt{\frac{4A}{3h}} \operatorname{arccosh} \left(\frac{1}{0.05} \right).$$

When $t = 0$, however, the solitary wave then has an elevation of 5% of its maximum at the toe of the beach. This is too much in a modeling context. Instead, the solitary solution (9) is imposed at $L + 5c$ so that the initial wave is on a horizontal bottom.

Figure 9 shows the snapshots of the water surface at $t=16, 18$, and 18.6 from BIM and WAVECLAW with $B=0$ and $1/15$. When the wave is smooth at $t=16$,

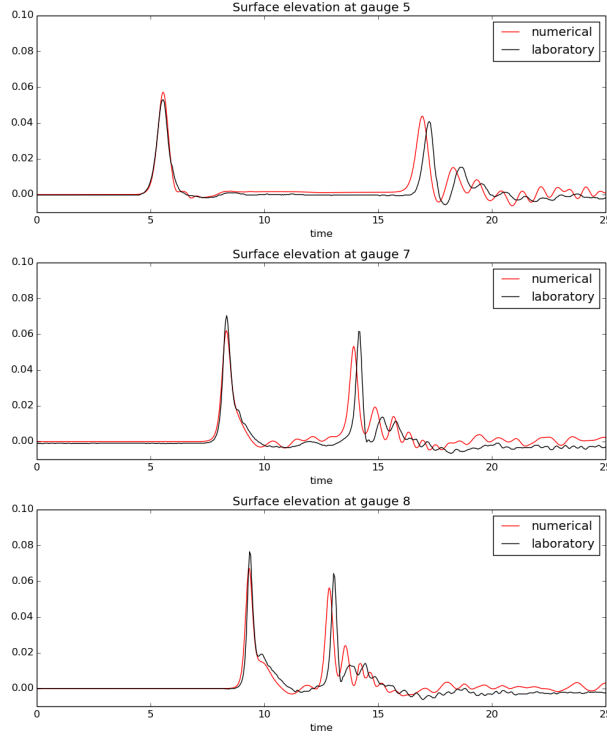


Figure 8: Water surface elevation at gauges 5,7 and 8 for $A/h = 0.269$ case.

the WAVECLAW results are almost identical. At the break point, $t = 18.6$, larger differences are observed. If $B = 0$, the wave speed is slightly faster than the BIM result, but the wave amplitude is similar. When $B = 1/15$, the wave speed matches the BIM results better, but the amplitude is slightly smaller. In
185 general, the computational results are rather similar with $B = 0$ and $1/15$.

The numerical simulations of the WAVECLAW are compared with the pre-existing softwares. GEOCLAW software [6] is chosen as a reference to the shallow water equations. The Boussinesq-type equation solvers such as FUNWAVE [12],
190 GLOBOUSS [25] and the Serre type [15], have also been used for comparison. . In the computations the original Serre's equations are enhanced by adding the Schäffer et al. (1995) [26] terms.

In Figure 10, snapshots from different numerical models are shown at $t=15$, 17 and 18. At $t=15$, the computational results from different numerical tools

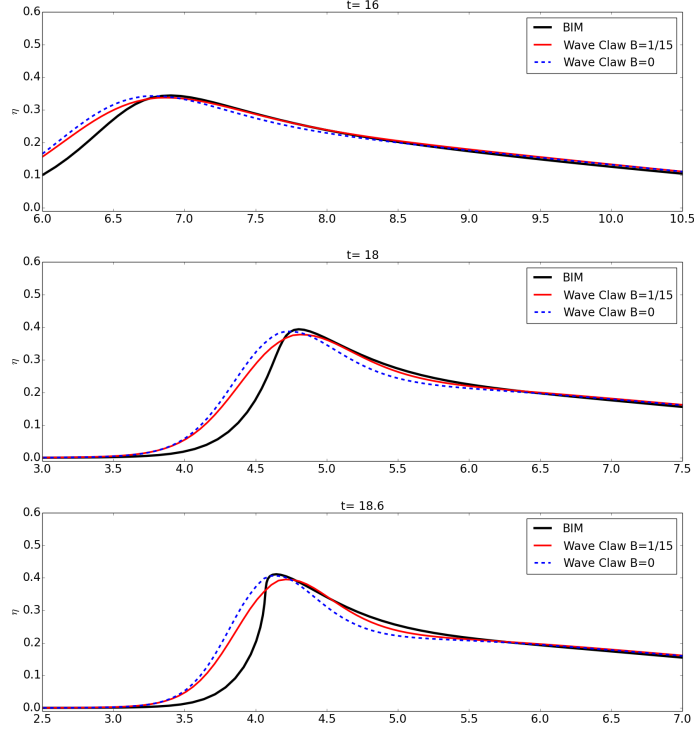


Figure 9: Snapshots of BIM and WAVECLAW with $B=0$ and $1/15$ at $t=16$, 18 and 18.6 .

show slightly different results, but the general pattern is similar. At $t=17$, some discrepancies are observed into two groups, and GLOBOUSS and FUNWAVE are analogous meanwhile WAVECLAW and Serre's results are alike. The wave amplitudes computed by GLOBOUSS and FUNWAVE, are more than 10 % larger than BIM. The wave amplitude continues to increase with GLOBOUSS and FUNWAVE simulations, and the difference from the BIM result becomes larger at $t = 18$. The results from the Serre and WAVECLAW models are very similar to those of the BIM model. Especially, the wave amplitudes are correctly determined by these models.

5.1. Wave Breaking

In order to catch wave breaking in a heuristic fashion, a threshold on $\epsilon_B := \eta/h$ is applied to the WAVECLAW. When the threshold is reached, the wave

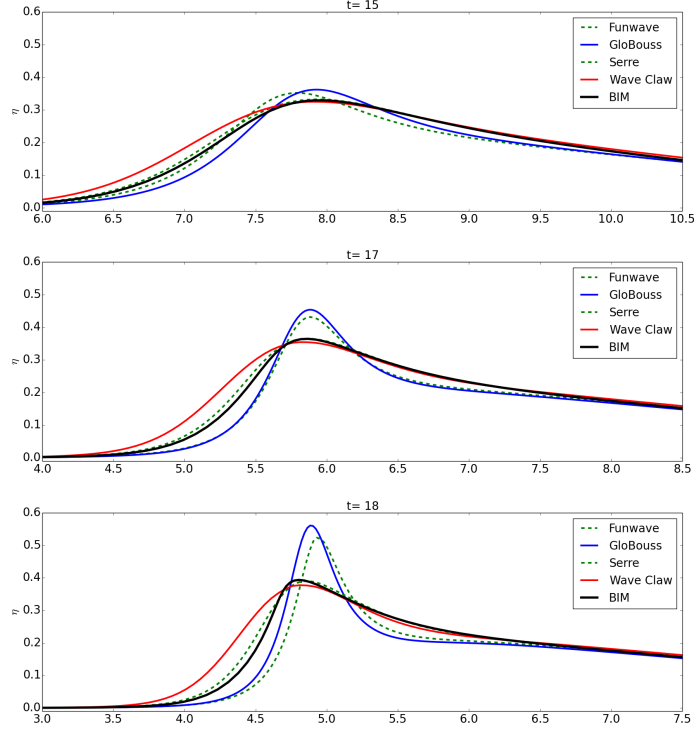


Figure 10: Snapshots of BIM, Serre, GLOBOUSS, WAVECLAW and FUNWAVE at $t = 15$, 17 and 18. The WAVECLAW is used with $B=1/15$, and the Peregrine's form is used for GLOBOUSS.

breaking is supposed to be initiated, and the dispersive terms are suppressed. At the breaking, the set of equations is switched to the shallow water equations in the vicinity of the wave crest. In the numerical simulation of the WAVECLAW
 210 model, the ratio ϵ_B reaches the threshold 0.8 at $t = 14.9$ when the peak of the wave is at $x = 8.03227$ m. At this time, the wave breaking is assumed to start, and the governing equations are switched to the shallow water equations.

In Figure 11, snapshots are shown at $t=15$, 17, and 18.6 from BIM, WAVE-
 CLAW and SWE. At $t=15$, the difference between BIM and WAVECLAW is
 215 small, but the difference becomes noticeable in the wave shape and amplitude at $t = 17$ and 18.6 . As the governing equations are switched to the shallow water equations, the wave starts to form a shockfront, and the wave amplitude decreases.

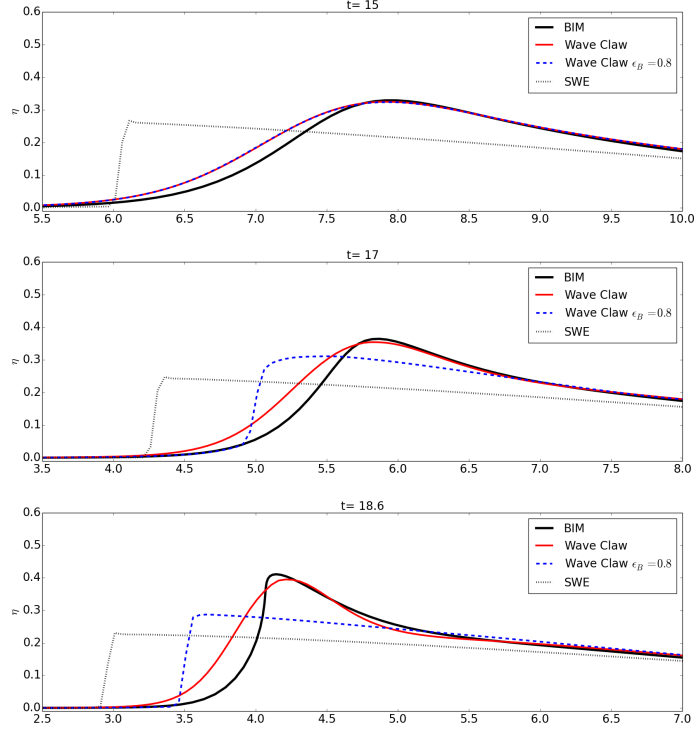


Figure 11: Comparison of BIM, WAVECLAW and SWE with $\epsilon = 0.8$ at $t = 15, 17$ and 18.6 .

Figure 12 shows the values of the wave breaking criteria at the given crest
 220 location. With BIM simulations, the wave starts breaking at $x = 4.09$ m. From WAVECLAW, the values at $x = 4.09$ m are $A/h = 1.97$, $u_s/c = 1.04$ and maximum angle= 39.1° where the maximum angle refers to the maximum slope of steepening wave.

5.2. Wave Energy

225 The wave energy is conserved when the wave is smooth, and decreases as the wave forms a shock or breaks. The wave energy expressions for the shallow water equations and Boussinesq equations are E_0 and $E_0 + E_1$ respectively, which are given in (11) and (12).

In Figure 13, the wave energy E_0 and $E_0 + E_1$ are shown. The energy
 230 denotes the aggregate of the wave energy in the entire computational domain at

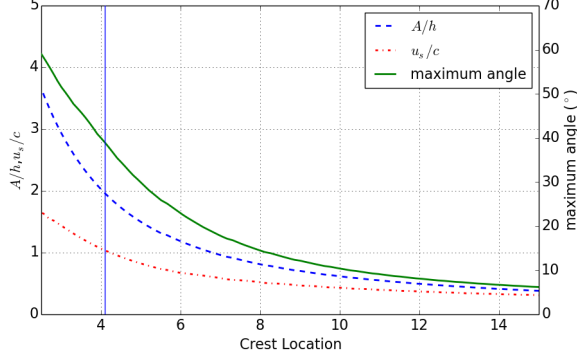


Figure 12: Plot of A/η , u_s/c and maximum angle of waves vs. crest location. BIM shows the wave break at $x = 4.09$.

the given crest location. On the left figure, the energy E_0 is well-preserved for the shallow water equations before the wave forms a shock, and then the energy dissipates after a shock is formed. On the right figure, $E_0 + E_1$ is well-preserved for the WAVECLAW, and this value decreases slightly as the wave steepens near the shoreline. When the threshold $\epsilon_B = 0.8$ is used, the energy $E_0 + E_1$ is well-preserved as shown on the right figure before the threshold is reached. When the crest is located at $x = 8.03227$ m with $\epsilon_B = 0.8$, the wave energy E_0 on the left figure does not decrease immediately. The energy E_0 is preserved for a while, then starts to decrease as a shock is formed.

6. Conclusion

What should the main conclusions be

- Dispersive Geoclaw works.
- Shallow water models and composite Boussinesq/NLSW models may give large errors in breaking point and wave shape
- Breaking does not really occur before the local amplitude is much higher than 0.8 time the depth – a limit that is inspired by the existence of

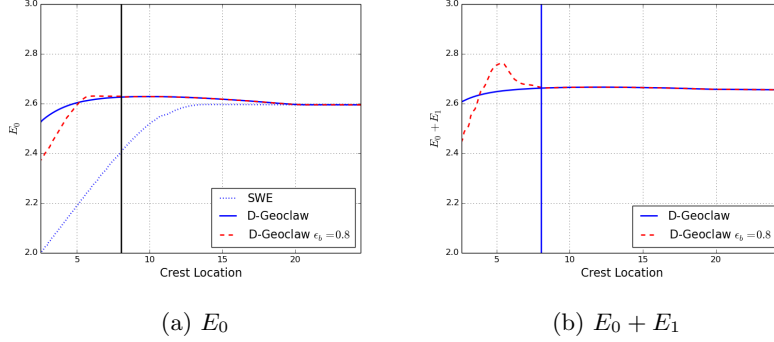


Figure 13: Energy plots of SWE and WAVECLAW. The vertical line is at $x = 8.03227$ m where $\epsilon_B = 0.8$, and the governing equations are switched to the SWE from the Boussinesq equations.

solitary wave solution in full potential theory. The 0.8 limit may be better on even gentler slopes.

- Effects of nonlinearities in the dispersion does influence the solution markedly, when accumulated up to the point of breaking.

References

- [1] D. H. Peregrine, Long waves on a beach, *Journal of Fluid Mechanics* 27 (04) (1967) 815–827.
- [2] P. A. Madsen, O. R. Sørensen, A new form of the Boussinesq equations with improved linear dispersion characteristics. Part 2. A slowly-varying bathymetry, *Coastal Engineering* 18 (3) (1992) 183–204.
- [3] O. Nwogu, Alternative form of Boussinesq equations for nearshore wave propagation, *Journal of Waterway, Port, Coastal, and Ocean Engineering*.
- [4] P. J. Lynett, T.-R. Wu, P. L.-F. Liu, Modeling wave runup with depth-integrated equations, *Coastal Engineering* 46 (2) (2002) 89–107.

- [5] G. Wei, J. T. Kirby, Time-dependent numerical code for extended Boussinesq equations, *Journal of Waterway, Port, Coastal, and Ocean Engineering* 121 (5) (1995) 251–261.
- [6] Clawpack Development Team, Clawpack software, version 5.3.1 (2016).
 265 URL <http://www.clawpack.org>
- [7] H. A. Schäffer, P. A. Madsen, R. Deigaard, A Boussinesq model for waves breaking in shallow water, *Coastal Engineering* 20 (3) (1993) 185–202.
- [8] R. J. LeVeque, Wave propagation algorithms for multidimensional hyperbolic systems, *Journal of Computational Physics* 131 (2) (1997) 327–353.
- [9] D. L. George, Augmented Riemann solvers for the shallow water equations
 270 over variable topography with steady states and inundation, *Journal of Computational Physics* 227 (6) (2008) 3089–3113.
- [10] M. J. Berger, D. L. George, R. J. LeVeque, K. T. Mandli, The GeoClaw software for depth-averaged flows with adaptive refinement, *Adv. Water Res.* 34 (2011) 1195–1206.
 275 URL www.clawpack.org/links/papers/awr11
- [11] M. Tissier, P. Bonneton, F. Marche, F. Chazel, D. Lannes, Serre Green-Naghdi modelling of wave transformation breaking and run-up using a high-order finite-volume finite-difference scheme, *Coastal Engineering Proceedings* 1 (32) (2011) 13.
 280
- [12] F. Shi, J. T. Kirby, J. C. Harris, J. D. Geiman, S. T. Grilli, A high-order adaptive time-stepping tvd solver for Boussinesq modeling of breaking waves and coastal inundation, *Ocean Modelling* 43 (2012) 36–51.
- [13] D. Dutykh, T. Katsaounis, D. Mitsotakis, Finite volume methods for unidirectional dispersive wave models, *International Journal for Numerical Methods in Fluids* 71 (6) (2013) 717–736.
 285

- [14] R. J. LeVeque, Finite volume methods for hyperbolic problems, Vol. 31, Cambridge university press, 2002.
- [15] F. Løvholt, P. Lynett, G. K. Pedersen, Simulating run-up on steep slopes with operational Boussinesq models; capabilities, spurious effects and instabilities, *Nonlin. Processes Geophys.* 20 (2013) 379–395.
- [16] F. Løvholt, G. Pedersen, G. Gisler, Oceanic propagation of a potential tsunami from the La Palma Island, *J. Geophys. Res.* 113 (2008) C09026, doi:10.1029.
- [17] C. E. Synolakis, The runup of solitary waves, *Journal of Fluid Mechanics* 185 (1987) 523–545.
- [18] V. V. Titov, C. E. Synolakis, Modeling of breaking and nonbreaking long-wave evolution and runup using VTCS-2, *Journal of Waterway, Port, Coastal, and Ocean Engineering* 121 (6) (1995) 308–316.
- [19] M. Tonelli, M. Petti, Hybrid finite volume–finite difference scheme for 2DH improved Boussinesq equations, *Coastal Engineering* 56 (5) (2009) 609–620.
- [20] P. J. Lynett, Nearshore wave modeling with high-order Boussinesq-type equations, *Journal of Waterway, Port, Coastal, and Ocean Engineering*.
- [21] M. Tissier, P. Bonneton, F. Marche, F. Chazel, D. Lannes, A new approach to handle wave breaking in fully non-linear Boussinesq models, *Coastal Engineering* 67 (2012) 54–66.
- [22] M. Matsuyama, M. Ikeno, T. Sakakiyama, T. Takeda, A study of tsunami wave fission in an undistorted experiment, *Pure and Applied Geophysics* 164 (2-3) (2007) 617–631.
- [23] P. A. Madsen, O. Sørensen, H. Schäffer, Surf zone dynamics simulated by a Boussinesq type model. part i. model description and cross-shore motion of regular waves, *Coastal Engineering* 32 (4) (1997) 255–287.

- [24] M. Briggs, Runup of solitary waves on a vertical wall, Coastal Hydraulics Laboratory.
 315 URL <http://chl.erd.c.usace.army.mil/chl.aspx?p=s&a=Projects;36>
- [25] F. Løvholt, G. Pedersen, S. Glimsdal, Coupling of dispersive tsunami propagation and shallow water coastal, Open Oceanography Journal 4 (2010) 71–82.
- [26] H. A. Schäffer, P. A. Madsen, Further enhancements of Boussinesq-type
 320 equations, Coastal Engineering 26 (1) (1995) 1–14.
- [27] C. Su, C. Gardner, Korteweg-de Vries equation and generalizations. III. derivation of the Korteweg-de Vries equation and Burgers equation, Journal of Mathematical Physics 10 (3) (1969) 536–539.
- [28] T. B. Benjamin, J. L. Bona, J. J. Mahony, Model equations for long waves
 325 in nonlinear dispersive systems, Philosophical Transactions of the Royal Society of London A: Mathematical, Physical and Engineering Sciences 272 (1220) (1972) 47–78.

Appendix A. Comparison of the Boussinesq equations

A class of the Boussinesq-type equations can be written in the following form,

$$(H)_t + (Hu)_x = 0, \quad (\text{A.1})$$

$$(Hu)_t + \left(Hu^2 + \frac{gH}{2} \right)_x + gHh_x + \psi = 0, \quad (\text{A.2})$$

where ψ represents dispersion terms. If

$$\psi = \frac{Hh^2}{6}u_{xxt} - \frac{Hh}{2}(hu)_{xxt}, \quad (\text{A.3})$$

then these are called the Peregrine’s equations.

The Boussinesq equations by Schäffer and Madsen [26] can be approximately reduced to the Peregrine's form when $B = 0$. Since $H = h + \eta$, the Madsen's dispersion term (5) can be written as,

$$\begin{aligned}
\psi &= \frac{1}{6}h^3 \left(\frac{Hu}{h} \right)_{xxt} - \frac{1}{2}h^2(Hu)_{xxt} \\
&= \frac{1}{6}h^3 u_{xxt} + \frac{1}{6}h^3 \left(\frac{\eta u}{h} \right)_{xxt} - \frac{1}{2}h^2(hu)_{xxt} - \frac{1}{2}h^2(\eta u)_{xxt} \\
&= \frac{Hh^2}{6}u_{xxt} - \frac{Hh}{2}(hu)_{xxt} \\
&\quad - \frac{\eta h^2}{6}u_{xxt} + \frac{h^3}{6} \left(\frac{\eta u}{h} \right)_{xxt} + \frac{\eta h}{2}(hu)_{xxt} - \frac{h^2}{2}(\eta u)_{xxt} \quad (\text{A.4}) \\
&= \frac{Hh^2}{6}u_{xxt} - \frac{Hh}{2}(hu)_{xxt} + \mathcal{O}(\epsilon).
\end{aligned}$$

330 Because the last four terms in (A.4) are $\mathcal{O}(\epsilon)$. The dispersion terms of Schäffer and Madsen are approximately same as the Peregrine's. Because of the higher order terms in (A.4), Schäffer and Madsen's wave model has lower peak at the breaking than Peregrine's model.

Now use $H = h + \eta$ and $\eta_t = H_t = -(Hu)_x$, and assume η_{xx} is small. Then ψ can be rewritten as

$$\begin{aligned}
\psi &= \frac{1}{6}h^3 \left(\frac{Hu}{h} \right)_{xxt} - \frac{1}{2}h^2(Hu)_{xxt} \\
&= -Hhh_x u_{xt} - \frac{1}{3}Hh^2 u_{xxt} - Hh\eta_x u_{xt} \\
&\quad - \frac{1}{6}Hh\eta u_{xxt} + \frac{1}{6}h\eta^2 u_{xxt} + h\eta(h + \eta)_x u_{xt} + \frac{1}{6}h^3 \left(\frac{\eta u}{h} \right)_{xxt}
\end{aligned}$$

Meanwhile

$$\begin{aligned}
\left(\frac{\eta u}{h} \right)_{xxt} &= -\frac{2h_x}{h^2}\eta u_{xt} + \frac{2}{h}\eta_x u_{xt} + \frac{1}{h}\eta u_{xxt} + \frac{2h_x}{h^2}(Hu)_x u_x \\
&\quad - \frac{2}{h}(Hu)_{xx} u_x - \frac{1}{h}(Hu)_x u_{xx}.
\end{aligned}$$

Therefore ψ reduces to

$$\begin{aligned}
\psi &= Hh\eta_x u_{xt} + \left(\frac{2}{3}h_x\eta - \frac{2}{3}h\eta_x \right) hu_{xt} \\
&\quad + \frac{1}{6}h^3 \left(\frac{2h_x}{h^2}(Hu)_x u_x - \frac{2}{h}(Hu)_{xx}u_x - \frac{1}{h}(Hu)_x u_{xx} \right) \\
&= -Hhh_x u_{xt} - \frac{1}{3}Hh^2 u_{xxt} + \left(\frac{2}{3}h_x\eta - \frac{2}{3}h\eta_x \right) hu_{xt} \\
&\quad + \frac{1}{6}h^3 \left(\frac{2h_x}{h^2}(Hu)_x u_x - \frac{2}{h}(Hu)_{xx}u_x - \frac{1}{h}(Hu)_x u_{xx} \right)
\end{aligned}$$

Now consider the last term

$$\begin{aligned}
&\frac{1}{6}h^3 \left(\frac{2h_x}{h^2}(Hu)_x u_x - \frac{2}{h}(Hu)_{xx}u_x - \frac{1}{h}(Hu)_x u_{xx} \right) \\
&= \frac{1}{3}h \left(h_x(Hu)_x u_x - h(Hu)_{xx}u_x - \frac{h}{2}(Hu)_x u_{xx} \right) \\
&= \frac{1}{3}h \left(h_x(H_x u + H u_x) u_x - h(2H_x u_x + H u_{xx}) u_x - \frac{h}{2}(H_x u + H u_x) u_{xx} \right) \\
&= \frac{1}{3}h \left(h_x H (u_x)^2 - 2H_x h (u_x)^2 - H h u_x u_{xx} - \frac{h}{2} H_x u u_{xx} - \frac{h}{2} H u_x u_{xx} \right) \\
&= \frac{1}{3}h \left((h_x H - 2H_x h) (u_x)^2 - \frac{3Hh}{2} u_x u_{xx} - \frac{h}{2} H_x u u_{xx} \right)
\end{aligned}$$

If we rearrange (5) and assume that $h_x\eta$, h_{xx} and η_{xx} are small, then the Madsen's dispersion terms can be written as

$$\psi \approx -Hhh_x u_{xt} - \frac{Hh^2}{3} u_{xxt} - Hh\eta_x u_{xt} - \frac{1}{6}Hh\eta u_{xxt} + \frac{1}{6}h^3 \left(\frac{\eta u}{h} \right)_{xxt}.$$

Since $\eta_t = -(Hu)_x$, we have

$$\left(\frac{\eta u}{h} \right)_{xxt} \approx \frac{2\eta_x}{h} u_{xt} + \frac{\eta}{h} u_{xxt} + \frac{2h_x}{h^2} (Hu)_x u_x - \frac{2}{h} (Hu)_{xx} u_x - \frac{1}{h} (Hu)_x u_{xx}.$$

Plugging in and dropping small terms yields to

$$\begin{aligned}
\psi &\approx -Hhh_x u_{xt} - \frac{Hh^2}{3} u_{xxt} - Hh\eta_x u_{xt} - \frac{1}{6} Hh\eta u_{xxt} \\
&\quad + \frac{h^2 \eta_x}{3} u_{xt} + \frac{h^2 \eta}{6} u_{xxt} + \frac{hh_x}{3} (Hu)_x u_x - \frac{h^2}{3} (Hu)_{xx} u_x - \frac{h^2}{6} (Hu)_x u_{xx} \\
&\approx -Hhh_x u_{xt} - \frac{Hh^2}{3} u_{xxt} - Hh\eta_x u_{xt} \\
&\quad + \frac{h^2 \eta_x}{3} u_{xt} + \frac{hh_x}{3} (Hu)_x u_x - \frac{h^2}{3} (Hu)_{xx} u_x - \frac{h^2}{6} (Hu)_x u_{xx}. \tag{A.5}
\end{aligned}$$

The Serre's equations of Su and Gardner [27] has the following dispersion terms,

$$\begin{aligned}
\psi &= -Hhh_x u_{xt} - \frac{Hh^2}{3} u_{xxt} - Hh\eta_x u_{xt} \\
&\quad - \frac{2}{3} Hh\eta u_{xxt} + \frac{Hh^2}{3} [(u_x)^2 - uu_{xx}]_x. \tag{A.6}
\end{aligned}$$

It is observed that (A.5) and (A.6) share common terms. Numerical results also show that Schäffer and Madsen's model is more similar to Serre's equations than Peregrine's equations.

Appendix B. Stability of the hybrid scheme

In order to investigate the stability of the proposed hybrid numerical scheme, we consider a linearized Benjamin-Bona-Mahony (BBM) equation (Benjamin et al., 1972 [28]), which is a class of the Boussinesq-type equations. The PDE is given as follows,

$$u_t + u_x = u_{txx}. \tag{B.1}$$

In order to apply the hybrid scheme, the equation (B.1) is rearranged as

$$(I - D^2)(u_t + u_x) + D^2 u_x = 0, \tag{B.2}$$

where $D = \partial_x$. Then we are required to solve the following PDE,

$$\begin{cases} u_t + u_x + S = 0, \\ (I - D^2) S = D^3 u. \end{cases} \tag{B.3}$$

When the hybrid scheme is applied, the advection equation

$$u_t + u_x = 0, \quad (\text{B.4})$$

is solved with the finite volume method, and then the fractional step method is applied to the following equation,

$$u_t + S = 0.$$

If we use the centered difference approximation of $O(\Delta x^2)$ accuracy, and the four-stage Runge-Kutta scheme for time stepping, then we have,

$$\begin{aligned} U_1 &:= u^n \\ U_2 &:= u^n - \frac{\Delta t}{2} S_1, \quad \text{where } (I - D^2)S_1 = D^3 U_1, \\ U_3 &:= u^n - \frac{\Delta t}{2} S_2, \quad \text{where } (I - D^2)S_2 = D^3 U_2, \\ U_4 &:= u^n - \Delta t S_3, \quad \text{where } (I - D^2)S_3 = D^3 U_3, \\ u^{n+1} &= u^n - \frac{\Delta t}{6} [S_1 + 2S_2 + 2S_3 + S_4], \quad \text{where } (I - D^2)S_4 = D^3 U_4. \end{aligned}$$

For each step, S_i 's are computed from

$$(S_i)_j - \frac{(S_i)_{j+1} - 2(S_i)_j + (S_i)_{j-1}}{\Delta x^2} = \frac{u_{j+2} - 2u_{j+1} + 2u_{j-1} - u_{j-2}}{2\Delta x^3}.$$

In order to investigate the stability with von Neumann analysis, replace $u_j = e^{i\xi j \Delta x}$ and $(S_1)_j = \beta e^{i\xi j \Delta x}$. Simplification gives

$$\begin{aligned} \beta \left(1 - \frac{-2 + 2 \cos(\xi \Delta x)}{\Delta x^2} \right) &= \frac{\sin(2\xi \Delta x) - 2 \sin(\xi \Delta x)}{\Delta x^3} i, \\ \beta &= \frac{-2 \sin(\xi \Delta x)(1 - \cos(\xi \Delta x))}{\Delta x^3 + 2\Delta x(1 - \cos(\xi \Delta x))} i. \end{aligned}$$

Note that β is a purely imaginary number. If we replace the four-stage Runge-

Kutta scheme with $u_j = e^{i\xi j \Delta x}$ and $(S_1)_j = \beta e^{i\xi j \Delta x}$, then we have

$$\begin{aligned} S_1 &= \beta e^{i\xi j \Delta x}, \quad U_2 = \left(1 - \frac{\Delta t \beta}{2}\right) e^{i\xi j \Delta x} \\ S_2 &= \beta \left(1 - \frac{\Delta t \beta}{2}\right) e^{i\xi j \Delta x}, \quad U_3 = \left(1 - \frac{\Delta t \beta}{2} + \frac{(\Delta t \beta)^2}{4}\right) e^{i\xi j \Delta x} \\ S_3 &= \beta \left(1 - \frac{\Delta t \beta}{2} + \frac{(\Delta t \beta)^2}{4}\right) e^{i\xi j \Delta x}, \\ U_4 &= \left(1 - \Delta t \beta + \frac{(\Delta t \beta)^2}{2} - \frac{(\Delta t \beta)^3}{4}\right) e^{i\xi j \Delta x}, \\ S_4 &= \beta \left(1 - \Delta t \beta + \frac{(\Delta t \beta)^2}{2} - \frac{(\Delta t \beta)^3}{4}\right) e^{i\xi j \Delta x}. \end{aligned}$$

Thus the growth factor $g(\xi)$ is

$$\begin{aligned} g(\xi) &= 1 - \frac{\Delta t}{6} \left[\beta + 2\beta \left(1 - \frac{\Delta t \beta}{2}\right) + 2\beta \left(1 - \frac{\Delta t \beta}{2} + \frac{(\Delta t \beta)^2}{4}\right) \right. \\ &\quad \left. + \beta \left(1 - \Delta t \beta + \frac{(\Delta t \beta)^2}{2} - \frac{(\Delta t \beta)^3}{4}\right) \right] \\ &= 1 - \frac{1}{6} \left(6\Delta t \beta - 3(\Delta t \beta)^2 + (\Delta t \beta)^3 - \frac{(\Delta t \beta)^4}{4} \right). \end{aligned}$$

Since β is an imaginary number, let $\Delta t \beta = \gamma i$ for some real γ , and then we have

$$\begin{aligned} g(\gamma) &= 1 - \frac{1}{2}\gamma^2 + \frac{\gamma^4}{24} + \left(\frac{\gamma^3}{6} - \gamma\right) i \\ |g(\gamma)|^2 &= 1 + \frac{1}{4}\gamma^4 + \frac{\gamma^8}{24^2} - \gamma^2 + \frac{\gamma^4}{12} - \frac{\gamma^6}{24} + \gamma^2 + \frac{\gamma^6}{36} - \frac{\gamma^4}{3} \\ &= 1 - \frac{1}{72}\gamma^6 + \frac{1}{576}\gamma^8. \end{aligned}$$

If $|\gamma| < 2\sqrt{2}$, then $|g(\gamma)| < 1$. The sufficient condition for stability is

$$\left| \frac{\Delta t}{\Delta x} \cdot \frac{\sin(\xi \Delta x)(1 - \cos(\xi \Delta x))}{\Delta x^2 + 2(1 - \cos(\xi \Delta x))} \right| < \sqrt{2}, \quad \text{for } \forall \xi \Delta x. \quad (\text{B.5})$$

For small Δx , this condition approximately reduces to

$$\frac{\Delta t}{\Delta x} < 2\sqrt{2}.$$

The CFL condition for the advection equation (B.4) is a sufficient condition.

Therefore, if the CFL condition is satisfied in the advection equation, the frac-

340 tional step is always stable with the suggested numerical scheme.

Appendix C. Energy estimates and dissipation

Appendix C.1. Velocity field

To derive the energy estimates for the Boussinesq-type equations, we define the depth-averaged velocity as,

$$\bar{u} = \frac{1}{H} \int_{-h}^{\epsilon\eta} u dz.$$

Then the velocity u can be expressed as $u = \bar{u} + \mu^2 u_1$ where

$$\int_{-h}^{\epsilon\eta} u_1 dz = 0. \quad (\text{C.1})$$

Then the kinematic boundary condition at the bottom and zero divergence implies

$$w = -h_x u - \bar{u}_x(z+h) + O(\mu^2).$$

Appendix C.2. Energy integrals

The potential energy density per horizontal area is

$$V = \int_{-h}^{\epsilon\eta} g z dz = \frac{1}{2} \epsilon^2 g \eta^2 - \frac{1}{2} g h^2,$$

where the last term $\frac{1}{2} g h^2$ is the equilibrium energy. The kinematic energy density has two contributions,

$$T = T_u + T_w; \quad T_u = \frac{1}{2} \epsilon^2 \int_{-h}^{\epsilon\eta} u^2 dz, \quad T_w = \frac{1}{2} \epsilon^2 \mu^2 \int_{-h}^{\epsilon\eta} w^2 dz.$$

For the horizontal part, T_u is

$$T_u = \frac{1}{2} \epsilon^2 \int_{-h}^{\epsilon\eta} u^2 dz = \frac{1}{2} \epsilon^2 \int_{-h}^{\epsilon\eta} \bar{u}^2 + 2\mu^2 \bar{u} u_1 + \mu^4 u_1^2 dz = \frac{1}{2} \epsilon^2 H \bar{u}^2 + O(\epsilon^2 \mu^4),$$

since \bar{u} is independent of z and by (C.1). Assuming $\frac{1}{H} \int_{-h}^{\epsilon\eta} u^2 dz = \bar{u}^2$, the vertical part is

$$\begin{aligned} T_u &= \frac{1}{2} \epsilon^2 \mu^2 \int_{-h}^{\epsilon\eta} h_x^2 u^2 + 2h_x u \bar{u}_x(z+h) + \bar{u}_x^2(z+h)^2 dz + O(\epsilon^2 \mu^4) \\ &= \frac{1}{2} \epsilon^2 \mu^2 H \left(h_x^2 \bar{u}^2 + H h_x \bar{u} \bar{u}_x + \frac{1}{3} H^2 \bar{u}_x^2 \right) + O(\epsilon^2 \mu^4). \end{aligned}$$

Thus the energy of a wave can be approximated as

$$E = \epsilon^2 (E_0 + \mu^2 E_1 + O(\mu^4))$$

where

$$E_0 = \frac{1}{2} (g\eta^2 + H\bar{u}^2),$$

$$E_1 = \frac{1}{6}H^3\bar{u}_x^2 + \frac{1}{2}H^2h_x\bar{u}\bar{u}_x + \frac{1}{2}Hh_x^2\bar{u}^2.$$